Multimodal and multiplex spectral imaging of rat cornea *ex vivo* using a white-light laser source

Hiroki Segawa[1], Yuichi Kaji[2], Philippe Leproux[3], Vincent Couderc[3], Takeaki Ozawa[1] and Hideaki Kano[,4]*

[1] *Department of Chemistry, School of Science, The University of Tokyo, 7-3-1, Hongo, Bunkyo, Tokyo, 113-0033, Japan*
[2] *Graduate School of Comprehensive Human Science, University of Tsukuba,1-1-1 Tennodai, Tsukuba, Ibaraki, 305-8575, Japan*
[3] *Institut de Recherche XLIM, UMR CNRS No. 6172, 123 avenue Albert Thomas, 87060 Limoges CEDEX, France*
[4] *Institute of Applied Physics, University of Tsukuba,1-1-1 Tennodai, Tsukuba, Ibaraki, 305-8573, Japan*

Received zzz, revised zzz, accepted zzz
Published online zzz

Key words: Nonlinear optical imaging, Second harmonic generation, Third harmonic generation, Coherent anti-Stokes Rama scattering

We applied our multimodal nonlinear spectral imaging microscope to the measurement of rat cornea. We successfully obtained nonlinear signals of coherent anti-Stokes Raman scattering (CARS), third-order sum frequency generation (TSFG), and second harmonic generation (SHG). Depending on the nonlinear optical processes, the cornea tissue was visualized with different image contrast mechanism simultaneously. Due to white-light excitation, multiplex CARS and TSFG spectra were obtained. Combined multimodal and spectral analysis clearly elicited the inner structure of rat cornea with molecular structural information. This study indicates our multimodal nonlinear spectral microscope is a promising method for cell or tissue studies.

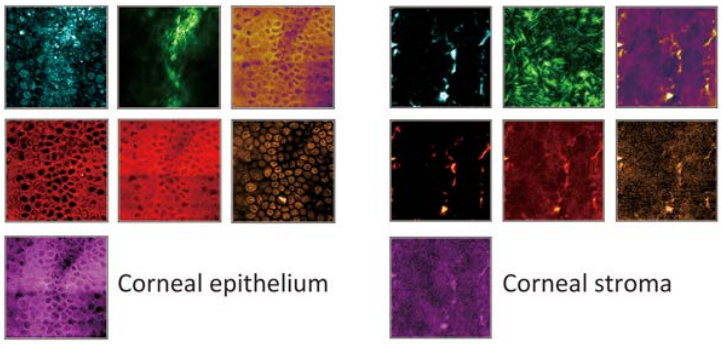

Multimodal nonlinear spectral images of rat cornea at corneal epithelium and corneal stroma in the lateral diraction. By the combinational analysis of different nonlinear processes, detailed molecular structural information is available without staing or labeling.

1. Introduction

In vivo and *in situ* visualization of biological tissue components without staining and molecular tagging are of considerable importance in biological and medical science. Optical coherence tomography [1] or confocal microscopy [2] are widely used for in-situ imaging of the biological tissue. Both two techniques are capable of capturing micrometer-resolution three-dimensional images from optical scattering media. However, they provide limited image-contrast and poor molecular specificity due to their contrast mechanism, which relies on spatial variations of refractive indices.

Recently, multiphoton microscopy has attracted much attention. Multiphoton microscopy is based on the nonlinear interactions between molecules and photons. Two or three photons from a pulsed near-infrared (NIR) laser source are focused onto a sample to generate one photon in the spectral range different from those of the input photons. The signal is generated from a tightly-focused confined volume resulting in three-dimensional sectioning capability. So far, various kinds of nonlinear optical processes such as two- or three-photon excited fluorescence[3,4], second- or third harmonics generation (SHG or THG) [5–11], sum-frequency generation (SFG)[12], third-order sum frequency generation (TSFG)[13], coherent anti-Stokes Raman scattering (CARS)[14–16] and stimulated Raman scattering (SRS)[17–19] have been applied to microscopy. Since these nonlinear optical processes simultaneously take place, we are able to combine various multiphoton mi-

* Corresponding author: e-mail hkano@bk.tsukuba.ac.jp, Phone: +81 29 853 5421, Fax: +00 999 999 999

Copyright line will be provided by the publisher

croscopic techniques[13,20]. This multimodality offers exclusive capabilities to obtain information on molecular composition, organization, and dynamics in an unstained or unlabeled tissue, which is not accessible using other noninvasivse methods.

By using a spectrometer, spectral imaging can also be performed using a single excitation laser source. In order to extend the spectral coverage of the excitation laser, a supercontinuum (SC) white-light source is applicable. The SC, or white-light laser source, can be generated by seeding laser pulses into a photonic crystal fiber (PCF) [!!Ranka et.al.〇 Optics Letters, Vol. 25, Issue 1, pp. 25-27 (2000)]. The temporal duration of SC are ranging from femtosecond to nanosecond time scale, depends on that of the seeding laser. In our previous study, we have developed tetra-modal (CARS, SHG, THG and TSFG) and multiplex microspectroscopy using subnanosecond NIR excitation (1064-1600 nm), and applied it to visualize living yeast cells[13]. The NIR excitation is also advantageous in particular to imaging of the tissue sample due to suppression of photodamage and large penetration depth.

In the present study, we evaluated the applicability of our multimodal multiphoton spectral microscope to imaging of the rat cornea *ex vivo*. The cornea is the transparent tissue, which is positioned at the front part of the eye. It functions as an external wall of the eye and a lens, and plays an important role in vision. The cornea is known to have a layered structure. Concerning the rat cornea, it consists of mainly four layers, corneal epithelium, corneal stroma, Descemet's membrame, and corneal endothelium. Although the cornea is transparent, previous studies of multiphoton microscopy succeeded in revealing the inner structure of cornea without staining by the use of SHG and THG[21,22]. CARS and two-photon autofluorescence (TPAF) were also applied to visualizing mouse cornea, and distributions of lipid and protein have been reported[23]. However, previous CARS study is focused only on the CH stretch vibrational modes, which provide poor and indirect information on molecular structure and conformation. Since our multimodal and multiphoton technique is capable of multiplex CARS spectral imaging in the molecular-fingerprint region (800-1800 cm^{-1}) as well as the CH stretch region, it possibly visualizes the detailed structure of cornea with plenty molecular structural information.

2. Experimental

2.1 Multimodal and multiplex spectral microscope

The schematic diagram of our setup is shown in Fig. 1. The detail is described elsewhere[13,24]. Briefly, the light source is a cw Q-switched microchip Nd:YAG laser. The temporal duration, output power, and repetition rate are 800 ps, 300 mW, and 33 kHz, respectively. The output beam is divided into two. The one is used directly (1064 nm) as the excitation radiation (ω_1). The other is used as seed laser pulses, which are introduced into a PCF to generate supercontinuum (white-light laser) (ω_2). With using a long-pass filter, only the near-infrared spectral component (>1064 nm) is exploited. Two radiations are superimposed by a notch filter, and are tightly focused by the microscope objective (Nikon CFI Plan Apo 60x/NA 1.2) in a custom-made microscope. The transmitted TSFG, SHG and CARS signals are collected by a water-dip microscope objective (Nikon Apo NIR 60x/NA 1.0). With use of a visible/NIR dichroic mirror, CARS in NIR, and TSFG and SHG in UV-visible are spectrally separated, and are detected by two spectrometers. The sample is mounted on a three-dimensional PZT stage, and the signal is acquired by raster scanning. The exposure time is 100 msec/pixel. The pixel size is 500 nm in the lateral direction and 1 μm in the axial direction.

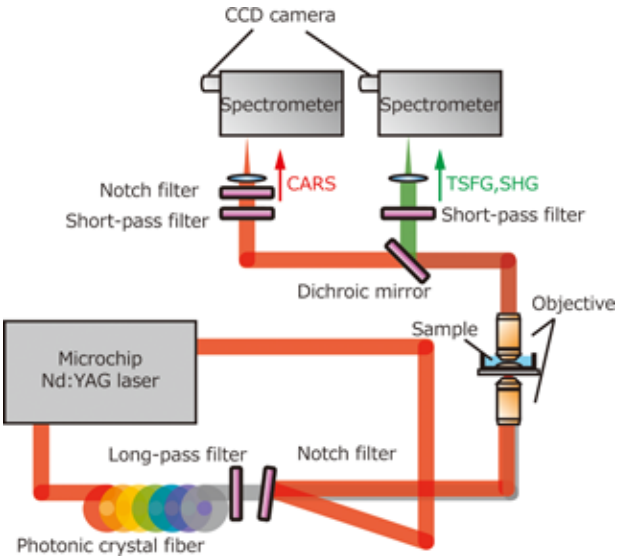

Figure 1 Schematic diagram of the setup of multimodal (TSFG, SHG and CARS) and multiplex spectral microscope.

2.2 Sample preparation of rat cornea

12- to 16-week-old male Long Evans rats, each weighing 250 to 400 g (Charles River Laboratories), were used. All animals were treated in accordance with the ARVO Statement for the Use of Animals in Ophthalmic and Vision Research. Experimental protocols were approved from the animal ethics review board in University of Tsukuba. Each rat was anesthetized by intraperitoneal injection of pentobarbital (25 mg/kg of body weight). Under an operating microscope, corneas of the both eyes were excised. The corneas were soaked in normal saline

Copyright line will be provided by the publisher

and then placed between a glass dish and a cover glass with epithelial side downward.

3. Results and discussion

Figures 2 (a-c) show spectral profiles of the signals due to multiple nonlinear optical processes in the UV-visible-NIR regions at three different corneal positions (a: corneal stroma, b: between corneal stroma and epithelium, c: corneal epithelium). Owing to the combined excitation with the SC and 1064-nm laser pulses, multiple nonlinear optical processes take place in the UV-visible-NIR regions. Hereafter, we assign the signal to each nonlinear optical process. The signal around 380 nm with a broad spectral profile is assigned to multiplex TSFG mainly due to $2\omega_1 + \omega_2$. It has been reported previously by our group[13], and the spectral profile is similar to the previous report. In the present study, it was hard to observe the THG signal at 355 nm ($3\omega_1$). This is because of the water-dip microscope objective for the signal collection, which has low transmittance in the UV region. There are another two signals in visible wavelength region. The signal at 532 nm with a sharp spectral profile is assigned to SHG ($2\omega_1$). According to previous studies[21], strong SHG signals are obtained from the collagen fibers. As described later, the SHG signal reflects the orientation and distribution of the collagen fibrils. The signal around 550 nm with a broad spectral profile is assigned to multiplex SFG due to $\omega_1 + \omega_2$, which in general provides similar information to that of SHG. In NIR region, sharp and dispersive spectral profiles are superimposed on the broad background. They are typical spectral profiles of the multiplex CARS spectrum. As shown in the upper axis in Fig. 2, almost all fundamental Raman bands are simultaneously observed by using the white-light Stokes pulses. The dispersive lineshapes are due to the interference of the vibrationally resonant CARS signal with the so-called nonresonant background[16,25].

Figures 3 shows the spectral profiles of the imaginary part of the CARS signal (Im[$\chi^{(3)}$]) after the noise reduction by using the singular value decomposition (SVD) analysis[26]. These Im[$\chi^{(3)}$] spectra were calculated by maximum entropy method (MEM)[24]. The MEM does not require any *a priori* knowledge of the vibrational bands but still is able to retrieve the phase information on the third-order nonlinear susceptibility $\chi^{(3)}$, whose imaginary part corresponds to ordinary (spontaneous) Raman spectra[27]. Therefore, the intensity of the retrieved band, Im[$\chi^{(3)}$], is proportional to the molecular concentration. In other words, each band can be evaluated quantitatively. The Im[$\chi^{(3)}$] spectra show rich information on the molecular composition of cornea tissue. The strong band around 2900 cm^{-1} is assigned as the CH stretch vibrational modes. This broad band is the superposition of the CH_3 stretch vibrational mode (2932 cm^{-1} and 2871 cm^{-1}) and CH_2 stretch vibrational mode (2847 cm^{-1}). CH_2 stretch mode is widely used as the marker band of lipid molecules[14]. On the other hand, CH_3 stretch band is used for probing the distribution of both protein and lipid molecules. In the fingerprint region (800-1800 cm^{-1}) shown in Fig. 3(d)-(f), there are many bands correspond to various skeletal vibration modes, which are highly sensitive to the molecular

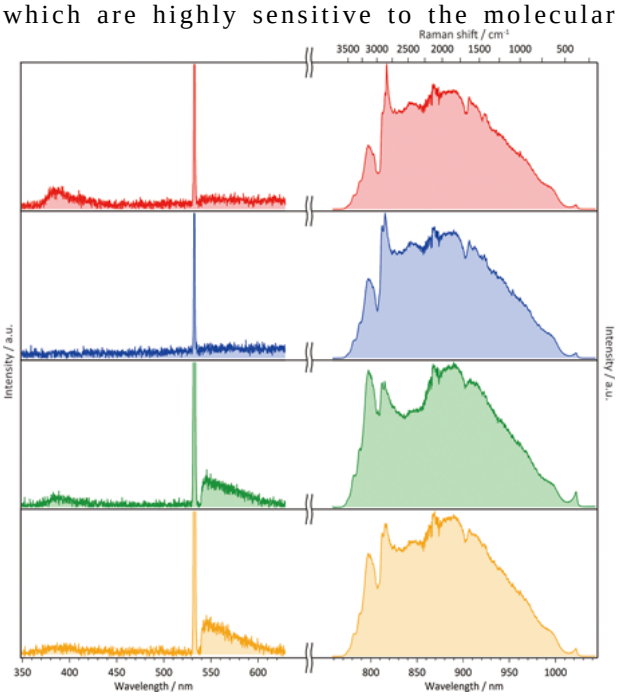

Figure 2 Spectral profiles of the nonlinear optical signals in the visible and NIR regions at three different corneal positions (a: corneal stroma, b: basement membrane, c: corneal epithelium).

Copyright line will be provided by the publisher

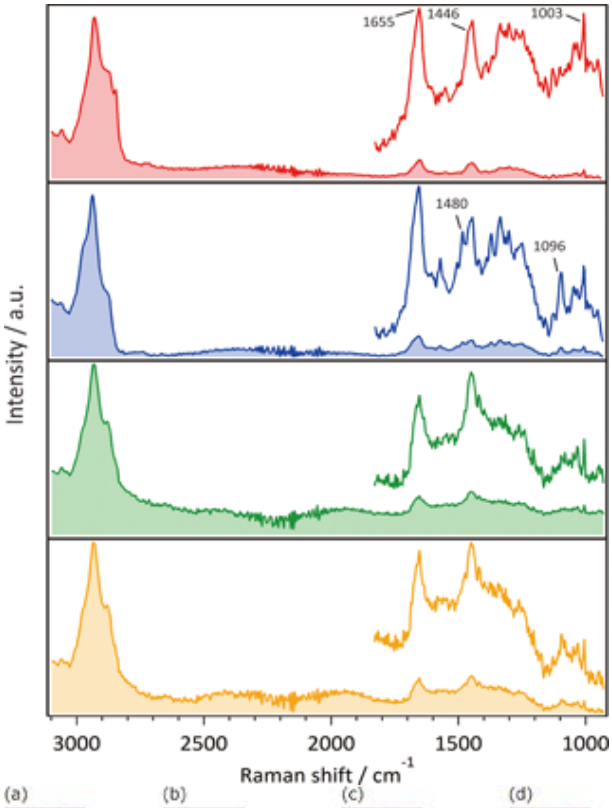

Figure 3 Spectral profiles of the imaginary part of the CARS signal (Im[$\chi^{(3)}$]) calculated by maximum entropy method at three different corneal positions (a: corneal stroma, b: basement membrane, c: corneal epithelium). Each position is indicated as the crosses (red: corneal stroma, blue: basement membrane, green: corneal epithelium) in Fig. 4(a). Spectral profiles in the fingerprint region are also depicted (d: corneal stroma, e: basement membrane, f: corneal epithelium).

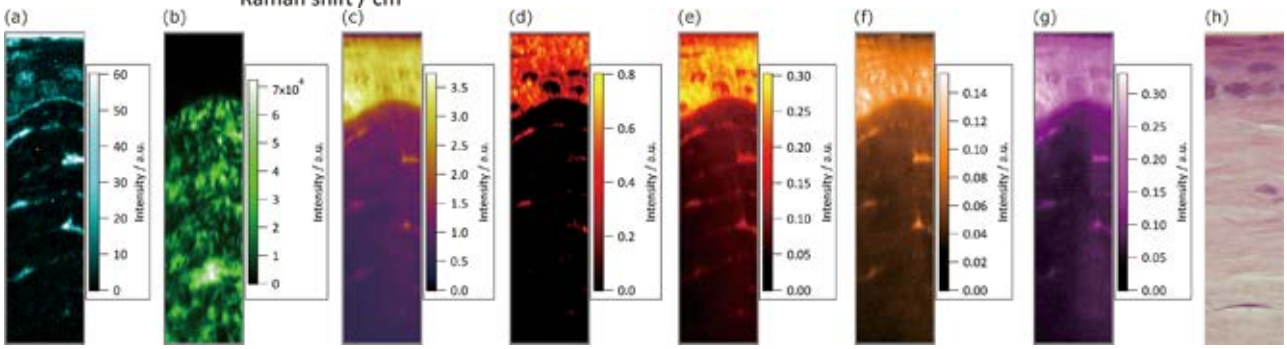

Figure 4 Multimodal and multiplex spectral imaging of the rat cornea tissue in the depth (axial; XZ) direction; (a) TSFG, (b) SHG, (c) CARS at CH_3 stretch, (d) CARS at CH_2 stretch, (e) CARS at CH bend, (f) CARS at purine-ring stretch, (g) CARS at phenylalanine residues, and (h) schematic of the rat cornea. The top part corresponds to the corneal epithelium. The image corresponds to 25x 175 μm^2. Three crosses (red: corneal stroma, blue: basement membrane, green: corneal epithelium) in Fig. 4(a) correspond to the position at which we extract the spectral profiles shown in Figs. 2 and 3.

structure. Although almost all bands are weak, our multiplex CARS technique with MEM and SVD analysis clearly reveals each vibrational mode. The band at 1655 cm^{-1} is assigned as the superposition of the C=C stretch of lipid chains and the amide I mode of proteins. The band at 1446 cm^{-1} is assigned to the CH bend mode, in which two CH bend modes, namely CH_2 scissors and CH_3 degenerate deformation, are overlapped[24]. The weak band around 1480 cm^{-1}, which locates at a shoulder of the band at 1446 cm^{-1}, is assigned to the purine-ring stretch mode[28]. This mode can be used as a marker band of purine bases such as adenine and guanine. The sharp band at 1003 cm^{-1} is assigned to the phenylalanine residues in proteins.

Multimodal and multiplex images were reconstructed by calculating the intensity of signal of each spectral band in obtained spectra such as Fig. 3 by multi-curve fitting with the sum of Gaussian functions. Figures 4(a-f) are constructed images of rat cornea in the depth (axial; XZ) direction. Each image corresponds to (a) TSFG, (b) SHG, (c) CARS at CH_3 stretch (protein, lipid), (d) CARS at CH_2 stretch (lipid), (e) CARS at CH bend (protein, lipid), (f) CARS at purine-ring stretch (purine base), and (g) CARS at phenylalanine residues (protein), respectively. To the best of our knowledge, this is the first

Copyright line will be provided by the publisher

report on the *ex vivo* multimodal tissue imaging with the use of the fingerprint CARS spectrum. The scanning area of these images was 25 μm in the lateral direction and 175 μm in the depth direction. Due to NIR excitation, deeply penetrated images of cornea were successfully obtained. The acquisition time of these images was about 15 min. It should be noted that the limitation of the penetration depth of this optical system is determined by motion range of the PZT stage rather than the scattering of the excitation radiations. Depending on the nonlinear optical processes and vibrational resonances, we are able to simultaneously obtain various images with different information. In Fig. 4(a)-(g), two layers are visualized, namely corneal epithelium and corneal stroma (see Fig. 4(h)). The upper and lower regions in Fig. 4(a)-(g) correspond to corneal epithelium and corneal stroma, respectively. In corneal epithelium, strong CARS signals were observed (Fig. 4(c)-(g)). This structure was assigned as epithelial cells because all lipid, protein and purine base CARS signals were obtained. As discussed in detail later, TSFG signals were also obtained from some epithelial cells (Fig. 4(a)). In corneal stroma, SHG image (Fig. 4(b)) visualized the structure different from that observed by the other images. This SHG image indicates the distribution of collagen fibers because corneal stroma contains a lot of collagen fibrils, which generate strong SHG signals[21]. TSFG and CARS images (Fig. 4(a) and (c)-(g)) visualized the thin structures. Similar to epithelial cells, all lipid, protein and purine base CARS signals were obtained from these flat structures. We thus assign these structures as keratocytes, which are kind of

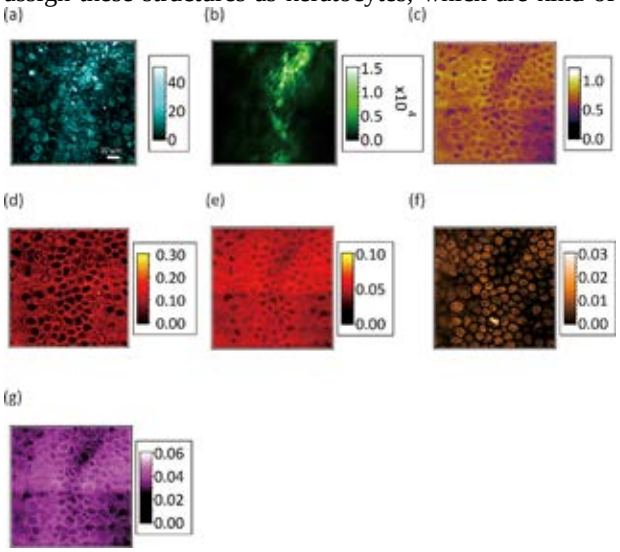

Figure 5 Multimodal and multiplex spectral imaging of the corneal epithelium in the in-place (lateral; XY) direction; (a) TSFG, (b) SHG, (c) CARS at CH3 stretch, (d) CARS at CH2 stretch, (e) CARS at CH bend, (f) CARS at purine-ring stretch, (g) CARS at phenylalanine residues. The image corresponds to 100x100 μm2.

a fibroblast activated only when the cornea was damaged. Keratocytes are pressed flat by surrounding collagen fibers. Due to this structure, interface-sensitive TSFG signals were detected at keratocytes. At the interface of corneal epithelium and stroma, a thin layer is clearly observed in Fig. 4(a). Interestingly, this thin layer is not highlighted in other images in Fig. 4(b-g). Taking account that the thin layer provides a protein-rich spectral profile (Fig. 3(b)), this structure is assigned as the basement membrane. Since the basement membrane consists of less SHG-active type-IV collagen, it is not clearly visualized by SHG in Fig. 4(b). The top edge of Fig. 4(a) corresponds to the interface of the cornea tissue and cover glass.

In order to investigate visualized corneal structures in more detail, we obtained in-plane (lateral; XY) images of rat cornea. Figures 5(a-h) and 6(a-g) show the results of multimodal and multiplex spectral imaging in the lateral direction. Each figure corresponds to the depth positions at corneal epithelium (Fig. 5) and stroma (Fig. 6), respectively. The scanning area is 100x100 μm square. Since the spatial resolution in the lateral direction is better than that in the axial direction, complicated structures inside each layer were clearly visualized. First, CARS at CH_2 stretch vibrational mode (lipid) image (Fig. 5(d))

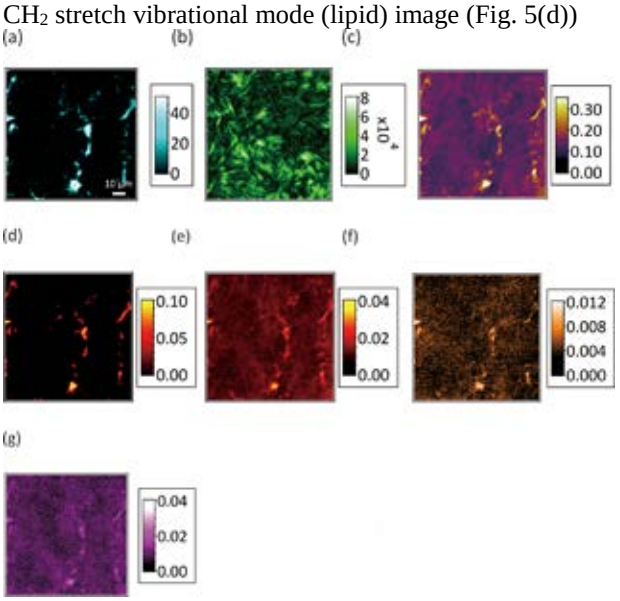

Figure 6 Multimodal and multiplex spectral imaging of the corneal stroma in the in-place (lateral; XY) direction; (a) TSFG, (b) SHG, (c) CARS at CH_3 stretch, (d) CARS at CH_2 stretch, (e) CARS at CH bend, (f) CARS at purine-ring stretch, and (g) CARS at phenylalanine residues. The image corresponds to 100x100 μm^2.

showed the honeycomb-like structure assigned as the cell membrane. It should be noted that cell membranes in general do not provide a strong CARS signal at CH_2 stretch in the case of single mammalian cells. The highlighted cell membrane image obtained by CARS CH_2 stretch is thus the characteristic of epithelial cells in tis-

Copyright line will be provided by the publisher

sue sample possibly due to the closely packing of each cell. Focusing on phenylalanine residue CARS image (protein, Fig. 5(g)), we can also recognize the honeycomb-like structure. In this image, moderate intensity of the CARS signal was observed from cytoplasm. CH_3 stretch and CH bend CARS images (fig. 5(c), (e)) are similar to the superposition of lipid (Fig. 5(d)) and protein (Fig. 5(g)) images. This means epithelial cells in cornea requires high concentration lipid and protein molecules. On the other hand, the signal distribution of CARS at purine ring vibrational mode (Fig. 5(f)) is totally different from above the other CARS images. In this image the cell membrane is not highlighted and the strong signal was observed at the center part of epithelial cells. Taking into consideration that the purine base is one of major components of DNA, nuclei of epithelial cells should be visualized in Fig. 5(f). The distribution of purine ring is inhomogeneous, and some cells show the doughnut-shaped structures. These structures possibly reflect the intranuclear distribution of RNA or nucleotide molecules such as ATP, all of which possess purine ring and are detectable by CARS at the purine ring vibrational mode.

Compared with CARS purine ring image (Fig. 5(f)), TSFG image (Fig. 5(a)) also shows similar intra-cellular structures. Since the contrast mechanism of TSFG is inhomogeneity of refractive index or nonlinear susceptibility, this image means that the inside of each epithelial cell is considerably inhomogeneous. In this image the speckle-like pattern is found. This pattern is not visualized in all the other images (Fig. 5(b)-(h)) On the other hand, SHG image (Fig. 5(b)) has clear contrast only around the upper-center part, where TSFG spot-like patterns are observed. Since the image is obtained near the boundary between corneal epithelium and stroma, and Fig. 5(b) is similar to Fig. 4(b), we consider that the part of epithelium is wavy, and stroma intrudes into the same depth position.

For corneal stroma, images are totally different from that obtained for corneal epithelium. As mentioned in the axial direction images, keratocytes are sparsely observed in Figs. 6(a) and (c-g). The keratocytes are compressed by the collagen fibrils, and show irregular cell shapes. The main component of corneal stroma is type-I collagen fibers, which are clearly observed with ordered arrangement in the SHG image (Fig. 6(b)). Since SHG is sensitive to the filamentous structure, it is reasonable that SHG signal from type-I collagen in stroma is clearly observed.

Lastly we performed three-dimensional (XYZ) multimodal multiplex spectral images of rat cornea *ex vivo*. Totally 21 lateral (XY) images (40x40 μm^2) are obtained with each 7.5 μm depth difference. The total acquisition time is about 3.9 hours. Figures 7 show some of 21-depth representative images, namely, 5 images with equidistant 22.5 μm depth positions from corneal epithelium (top) to stroma (bottom). The full movies of the image acquisition are available in supporting information (Fig. S1(a)-(g)). Since the optical axis of cornea tissue depends on the position of the sample, the laboratory coordinate (XYZ) is different from the optical axis of cornea. In Fig. 7, the left below part of the tissue is closer to the cover glass than the upper right. From the position of corneal epithelium to that of stroma, TSFG, SHG, and multiplex CARS images show characteristic depth dependence on their nonlinear optical responses and their chemical specificities. In particular, doughnut-like and spot-like patterns are observed at the center and the edge of corneal epithelium (See Fig. S(a)). These patterns probably detect the boundary of nuclei in three-dimensional view.

Copyright line will be provided by the publisher

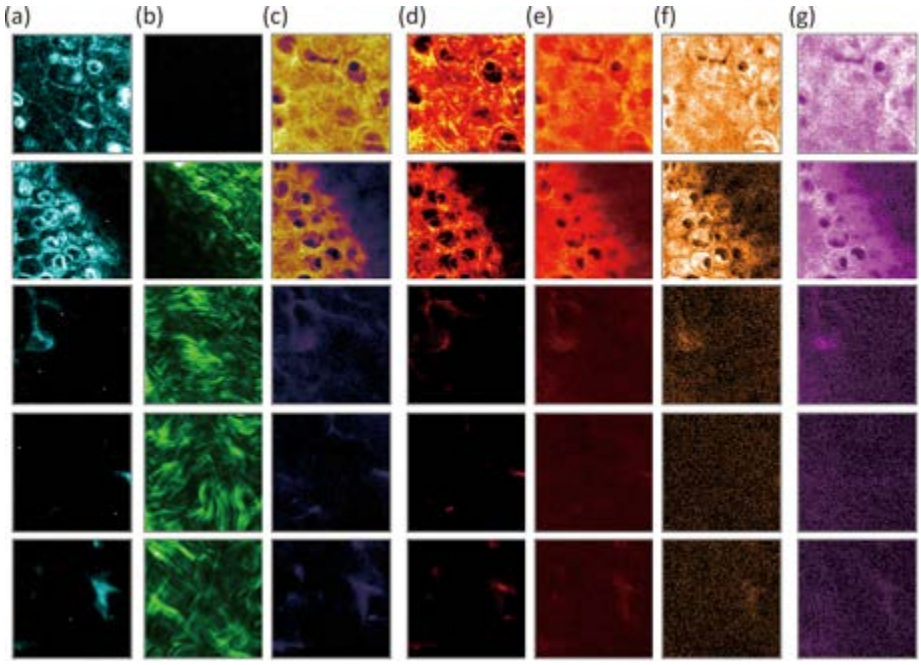

Figure 7 Multimodal and multiplex spectral imaging of the rat cornea tissue in the three-dimensional (XYZ) direction; (a) TSFG (Media 1), (b) SHG (Media 2), (c) CARS at CH_3 stretch (Media 3), (d) CARS at CH_2 stretch (Media 4), (e) CARS at CH bend (Media 5), (f) CARS at purine-ring stretch (Media 6), and (g) CARS at phenylalanine residues (Media 7). The image corresponds to 40x40 μm^2.

4. Conclusion

In this study we applied multimodal and multiplex spectral imaging with CARS, SHG and TSFG to *ex vivo* imaging of rat cornea. To the best of our knowledge, this is the first report on the *ex vivo* multimodal tissue imaging with the use of the fingerprint CARS spectrum. Depending on the nonlinear optical properties, cornea sample is visualized with different image contrast. TSFG visualizes nuclei and intra-nuclear structure in corneal epithelium. It also has clear contrast to the membrane like structure between corneal epithelium and corneal stroma. This structure was assigned as basement membrane. Label-free imaging of corneal basement membrane is important in the view point of diagnostics of corneal disorders, because special staining method is required to visualize this membrane. On the other hand, SHG clearly visualizes type-I collagen fibrils in corneal stroma. It is also important in diagnostics. Disorder of the arrangement of type-I collagen fiber also induce sever effect on vision. SHG can discriminate type-I (SHG active) from type-IV (less SHG active)) collagens. When corneal stroma is damaged, keratocytes grow proliferously. Subsequently, they produce type-IV collagen in order to infill the damaged area. Since type-IV collagen is less SHG active, we can monitor the wound healing process by SHG. This quaternary structure difference of collagens is possibly distinguished by CARS spectra. It is thus expected that we will be able to quantitatively evaluate the healing process because the intensity of $\mathrm{Im}[\chi^{(3)}]$ spectra obtained by MEM is quantitative and is proportion to the number of molecules in the focal volume. The multiplex CARS technique provides molecular specific vibrational images. The purine-ring stretch signal visualized cell nuclei and intra-nuclear DNA and RNA distribution. Thanks to the NIR excitation, photodamage is expected to be lowered and deeply penetrated images were obtained. This study proves that multimodal and mutilpex microspectroscopy provides valuable information on the microscopic properties of the cornea *ex vivo* and *in vivo* in the near future. The present acquisition time is precarious to apply to clinical use, but further improvement of the experiment setup possibly supports pathologists as a powerful label-free imaging tool. Although the measurement is performed in the transmission configuration, we can extend the system to the back-scattering configuration (epi detection). This technique provides huge potential for mini- or non-invasive, real-time cornea and other tissues study or diagnostics.

Author biographies Please see Supporting Information online.

Copyright line will be provided by the publisher

References

[1] W. Drexler, J.G. Fujimoto, Prog. Retin. Eye Res. **27**, 45–88 (2008).

[2] R.F. Guthoff, A. Zhivov, O., Clin. Experiment. Ophthalmol. **37**, 100–117 (2009).

[3] R. Sharma, L. Yin, Y. Geng, W.H. Merigan, G. Palczewska, K. Palczewski, D.R. Williams, J.J. Hunter, Biomed. Opt. Express **4**, 1285-1293 (2013).

[4] N.G. Horton, K. Wang, D. Kobat, C.G. Clark, F.W. Wise, C.B. Schaffer, C. Xu, Nat. Photonics **7**, 205–209 (2013).

[5] M. Savoldelli, M. Merano, D. Donate, O. Albert, V. Nuzzo, G. Mourou, J.-M. Legeais, K. Plamann, P.F.G. Rodríguez, J. Biomed. Opt. **12**, 1–11 (2007).

[6] S.-Y. Chen, H.-C. Yu, C.-K. Sun, I.-J. Wang, Infrared-based third and second harmonic generation imaging of cornea, J. Biomed. Opt. **14**, 1–7 (2009).

[7] S.-W. Teng, H.-Y. Tan, J.-L. Peng, H.-H. Lin, K.H. Kim, W. Lo, Y. Sun, W.-C. Lin, S.-J. Lin, S.-H. Jee, P.T.C. So, C.-Y. Dong, Invest. Ophthalmol. Vis. Sci. **47**, 1216–1224 (2006).

[8] J.M. Bueno, E.J. Gualda, A. Giakoumaki, P. Pérez-Merino, S. Marcos, P. Artal, Invest. Ophthalmol. Vis. Sci. **52**, 5325–5331 (2011).

[9] M. Han, G. Giese, J.F. Bille, Opt. Express, **13**, 5791-5797 (2005).

[10] A.T. Yeh, N. Nassif, A. Zoumi, B.J. Tromberg, Opt. Lett. **27**, 2082-2084 (2002).

[11] P. Steven, M. Hovakimyan, R.F. Guthoff, G. Hüttmann, O. Stachs, J. Cataract Refract. Surg. **36**, 2150–2159 (2010).

[12] V. Raghunathan, Y. Han, O. Korth, N.-H. Ge, E.O. Potma, Opt. Lett. **36**, 3891–3893 (2011).

[13] H. Segawa, M. Okuno, H. Kano, P. Leproux, V. Couderc, H.-O. Hamaguchi, Opt. Express **20**, 9551–9557 (2012).

[14] J.P. Pezacki, J. a Blake, D.C. Danielson, D.C. Kennedy, R.K. Lyn, R. Singaravelu, Nat. Chem. Biol. **7**, 137–145 (2011).

[15] C.-Y. Chung, J. Boik, E.O. Potma, Annu. Rev. Phys. Chem. **64**, 77–99 (2013).

[16] C.L. Evans, X.S. Xie, Annu. Rev. Anal. Chem., **1**, 883–909 (2008).

[17] C.W. Freudiger, W. Min, B.G. Saar, S. Lu, G.R. Holtom, C. He, J.C. Tsai, J.X. Kang, X.S. Xie, Science **1857**, 1857–1861 (2008).

[18] Y. Ozeki, W. Umemura, Y. Otsuka, S. Satoh, H. Hashimoto, K. Sumimura, N. Nishizawa, K. Fukui, K. Itoh, Nat. Photonics **6**, 845-851 (2012).

[19] M.C. Wang, W. Min, C.W. Freudiger, G. Ruvkun, X.S. Xie, Nat. Methods **8**, 135–138 (2011).

[20] S.H. Parekh, Y.J. Lee, K. a Aamer, M.T. Cicerone, Biophys. J., **99**, 2695–2704 (2010).

[21] F. Aptel, N. Olivier, A. Deniset-Besseau, J.-M. Legeais, K. Plamann, M.-C. Scbanne-Klein, E. Beaurepaire, Invest. Ophthalmol. Vis. Sci. **51**, 2459–2465 (2010).

[22] N. Olivier, F. Aptel, K. Plamann, M.-C. Schanne-Klein, E. Beaurepaire, Opt. Express **18**, 5028–5040 (2010).

[23] D.A. Ammar, T.C. Lei, M.Y. Kahook, O. Masihzadeh, Invest. Ophthalmol. Vis. Sci., **54**, 5258–5265 (2013).

[24] M. Okuno, H. Kano, P. Leproux, V. Couderc, J.P.R. Day, M. Bonn, H. Hamaguchi, Angew. Chem. Int. Ed. **49**, 6773–6777 (2010).

[25] E.E. Hoover, J.A. Squier, Nat. Photonics **7**, 93101 (2013).

[26] H.-J. van Manen, Y.M. Kraan, D. Roos, C. Otto, J. Phys. Chem. B **108**, 18762–18771 (2004).

[27] E.M. Vartiainen, H.A. Rinia, M. Müller, M. Bonn, Opt. Express, **14**, 3622–3630 (2006).

[28] A. Toyama, N. Hanada, J. Ono, E. Yoshimitsu, H. Takeuchi, J. Raman Spectrosc. **30**, 623–630 (1999).

Copyright line will be provided by the publisher